

Article

Exploring the Odd–Even Effect, Current Stabilization, and Negative Differential Resistance in Carbon-Chain-Based Molecular Devices

Lijun Wang ¹, Liping Zhou ^{1,*}, Xuefeng Wang ^{1,*}  and Wenlong You ²

¹ School of Physical Science and Technology, Soochow University, 1 Shizi Street, Suzhou 215006, China; 20214208055@stu.suda.edu.cn

² College of Physics, Nanjing University of Aeronautics and Astronautics, Nanjing 211106, China; wlyou@nuaa.edu.cn

* Correspondence: zhoulp@suda.edu.cn (L.Z.); wxf@suda.edu.cn (X.W.)

Abstract: The transport properties of molecular devices based on carbon chains are systematically investigated using a combination of non-equilibrium Green's function (NEGF) and density functional theory (DFT) first-principle methods. In single-carbon-chain molecular devices, a distinct even–odd behavior of the current emerges, primarily influenced by the density of states (DOS) within the chain channel. Additionally, linear, monotonic currents exhibit Ohmic contact characteristics. In ladder-shaped carbon-chain molecular devices, a notable current stabilization behavior is observed, suggesting their potential utility as current stabilizers within circuits. We provide a comprehensive analysis of the transport properties of molecular devices featuring ladder-shaped carbon chains connecting benzene-ring molecules. The occurrence of negative differential resistance (NDR) in the low-bias voltage region is noted, with the possibility of manipulation by adjusting the position of the benzene-ring molecule. These findings offer a novel perspective on the potential applications of atom chains.

Keywords: first principle; carbon chain; current-stabilizer behavior; odd–even effect; negative differential resistance (NDR)



Citation: Wang, L.; Zhou, L.; Wang, X.; You, W. Exploring the Odd–Even Effect, Current Stabilization, and Negative Differential Resistance in Carbon-Chain-Based Molecular Devices. *Electronics* **2024**, *13*, 1764. <https://doi.org/10.3390/electronics13091764>

Academic Editor: Elias Stathatos

Received: 8 April 2024

Revised: 24 April 2024

Accepted: 30 April 2024

Published: 2 May 2024



Copyright: © 2024 by the authors. Licensee MDPI, Basel, Switzerland. This article is an open access article distributed under the terms and conditions of the Creative Commons Attribution (CC BY) license (<https://creativecommons.org/licenses/by/4.0/>).

1. Introduction

The miniaturization of molecular devices has become a crucial frontier in nanoelectronics research [1–4], with atom chains emerging as prominent participants in this rapid advancement. As functional components, atom chains limit electron movement to a single dimension, unveiling distinctive transmission properties such as even–odd behaviors [5–9], length-dependent conductance [10], rectifying capabilities [11,12], and negative differential resistance (NDR) [8,11,13–16].

Notably, when atom chains are arranged in parallel and proximate configurations, they facilitate enhanced electron transport through constructive interference [17,18]. Mu et al. [19] conducted a comprehensive investigation into molecular devices composed of two silicon carbide chains that bridge gold electrodes, revealing that variations in the distances between these parallel chains can significantly influence the electronic transport properties of the devices. In the double-chain system with an interchain spacing of 2.884 Å, oscillating effects and negative differential resistance (NDR) phenomena were observed, with the NDR exhibiting variability in response to alterations in the chain length. Subsequently, Yun et al. [20] studied the transport properties of nanodevices composed of dual parallel carbon chains of varying lengths, sandwiched between two graphyne nanoribbon (GYNR) electrodes. Their investigations uncovered a pronounced current-stabilization effect.

Leveraging atom chains to link molecules within functional devices not only enables these systems with novel properties distinct from standalone atom chain devices, but also

generates a tunable platform, where device performance can be refined by modifying the atom chain lengths or molecules [21–28]. For instance, Han et al. [22] analyzed the transport properties of a molecular device consisting of a perylene molecule linked to two graphene nanoribbon (GNR) electrodes through carbon chains. Their findings highlighted the emergence of significant phenomena such as giant magnetoresistance, spin filtering, and NDR. In a related vein, Mu et al. [24] explored a single-molecule switch, where a dimethyldihydropyrene (DHP)/cyclophanediene (CPD) photosensitive molecule was linked to gold electrodes via carbon chains. The study demonstrated that the switching performance could be finely tuned by adjusting the carbon-chain length. Furthermore, Yao et al. [26] engineered a molecular device featuring a phenylene rotor, which, via a central carbon-chain axis, connects to two symmetric GNR electrodes, thereby enabling the modulation of NDR through phenylene rotation. Despite these advances, research on the electron transport properties of molecular devices assembled with a molecule interconnected by double parallel atom chains remains limited.

In this study, we probe the electron transport of a simple molecular device system based on carbon chains through first-principle methods. Initially, we examine carbon chains of varying lengths that bridge GNR electrodes. Subsequently, our focus shifts to a pair of parallel carbon chains positioned so closely that they form a unified, coherent structure, termed a ladder-shaped carbon chain. We investigate these ladder-shaped carbon chains of different lengths as they bridge GNR electrodes. Additionally, we explore a device where a benzene ring, a six-membered carbon structure, is connected to GNR electrodes via a ladder-shaped carbon chain. The insights garnered from this study are applicable to a broader range of molecular devices featuring various atomic chains.

2. Computational Methods

The geometry optimization and transport simulations for each system are conducted using the Atomistix Toolkits (ATK) software (Version: Q–2019. 12), which combines the nonequilibrium Green’s function (NEGF) method with density functional theory (DFT) [29,30]. Within this framework, the exchange–correlation interactions are addressed using the local density approximation (LDA) with Perdew–Zunger parametrization (LDA-PZ). A double- ζ orbital plus one polarization orbital (DZP) basis set is utilized for all atoms. The energy cutoff is 150 Ry, and the Brillouin zone sampling is defined by a $1 \times 1 \times 100$ mesh grid in k-space. The effects of the finite temperature distribution of electrons are taken into account, but the effects of the electron–phonon interaction are neglected. The electronic temperature is 300 K. The geometry has been optimized using the LBFGS method with a force-threshold criterion of 0.02 eV/Å. The device current is calculated by the Landauer–Büttiker formula:

$$I = G_0 \int T(E, V_b) [f_L(E) - f_R(E)] dE, \quad (1)$$

where G_0 is the quantum unit of the conductance, $T(E, V_b)$ is the transmission probability of the electron under energy E and bias voltage V_b . Furthermore, $f_L(E)$ and $f_R(E)$ correspond to the Fermi–Dirac distribution functions for the left and right electrodes, respectively.

3. Results and Discussion

We investigate carbon-atom chains connecting to two zigzag graphene nanoribbon (ZGNRs) electrodes. Note that the result for the ZGNRs of width number 6 is presented in the following, and the variation in width may affect quantitatively the results. Each carbon chain contains n atoms where n is between four and nine. For simplicity, the devices consisting of the abovementioned six carbon chains are named C_n with $n = 4, 5, 6, 7, 8,$ and 9 , as illustrated in Figure 1a. The current–voltage (I – V) characteristics of these devices are analyzed, as illustrated in Figure 1b. Notably, an even–odd effect in the current values is observed: devices with an odd number of carbon atoms exhibit significantly higher currents compared to those with an even number at the same applied voltage.

Furthermore, the currents for both odd- and even-numbered chains demonstrate a linear increase with voltage, suggesting their potential utility for achieving Ohmic contact in electronic applications.

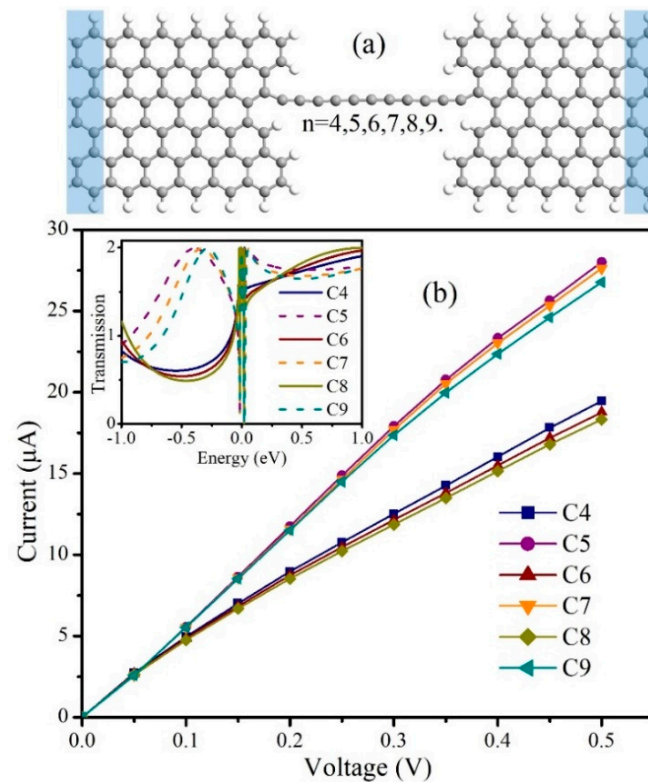


Figure 1. (a) Atomic structure of the single-carbon-chain devices. The blue rectangle areas indicate the left and right electrodes, between which is the central scattering region. (b) I–V curves of C4–C9. The inset is the zero-bias transmission spectra of C4–C9.

To better understand the I–V characteristics, we calculated the zero-bias transmission spectra of the devices, as shown in the inset of Figure 1b. All the devices have transmission peaks at the Fermi energy (E_F), where the transmission coefficient approaches two. This fact suggests that a minimal bias voltage is necessary to activate the electronic conduction channels to enter the current integration window, which in turn signifies a linear current increase with rising voltage under low-bias conditions. Particularly for devices with odd-numbered chains, the transmission peaks near E_F are more pronounced compared to those with even-numbered chains. Such a heightened transmission peak explains why odd-chain devices exhibit greater currents than their even-numbered counterparts, thereby elucidating the observed odd–even effects in their electrical behavior.

To elucidate the physical mechanism responsible for the observed odd–even phenomenon, we computed the total density of states (TDOS) for devices C4–C9, as depicted in Figure 2b. While these devices exhibit similar TDOS peaks around the Fermi energy (E_F), suggesting comparable I–V characteristics at first glance, this similarity contrasts with the distinct I–V behaviors actually observed in Figure 1b. Considering the TDOS profiles alone do not provide a satisfactory explanation for the odd–even phenomenon, we calculate the projected density of states (PDOS) at energies near the Fermi level (E_F). The results, illustrated in Figure 2c,d, reveal that the PDOS for the left (PDOS-L) and right (PDOS-R) regions display similar transmission peaks around E_F across all six device configurations, which similarly fail to clarify the odd–even behavior. The resemblance between PDOS-L, PDOS-R, and TDOS, particularly around E_F , is consistent across the devices, underscoring that the PDOS profiles, much like the TDOS, are not indicative of the distinct current variations observed between devices with odd and even numbers of carbon atoms. This

observation suggests that the density of states projected to the chain channel (PDOS-chain) for all the devices may play an important role in the transmission probability. As shown in Figure 3, the PDOS-chain exhibits distinct variations among the six structures, particularly around the Fermi energy. For devices with odd-numbered carbon chains, a prominent peak is observed at E_F , while devices with even-numbered chains display two smaller peaks. This indicates that devices with odd-numbered chains possess a higher density of carriers at E_F , enhancing their electron transport capabilities and resulting in higher current levels compared to their even-numbered counterparts. As a consequence, the PDOS-chain is identified as a critical factor in understanding the transport properties, where the coupling between the ZGNRs and the chain channels plays a dominant role in manifesting the odd–even phenomenon.

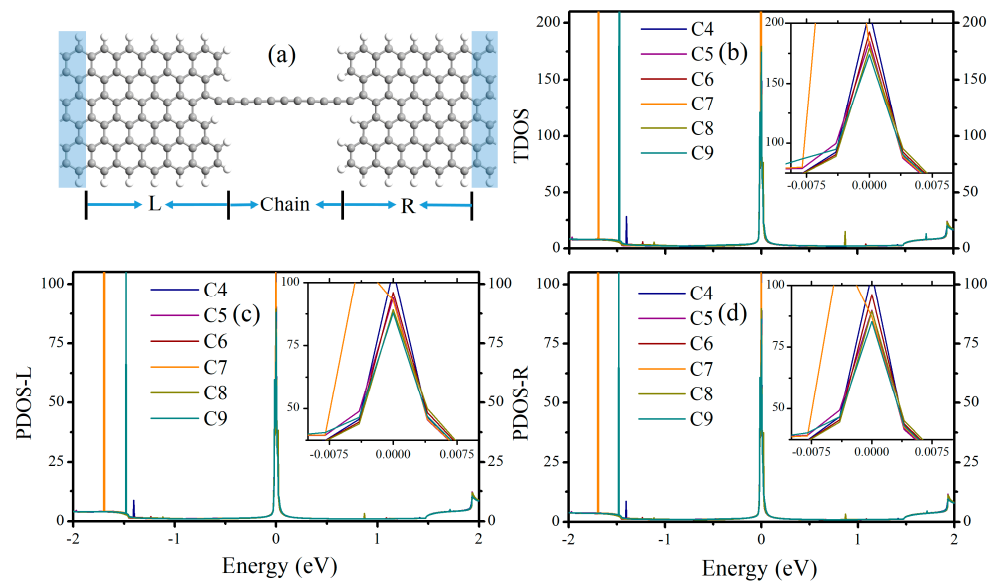


Figure 2. (a) The atomic structure of device C9 is shown as an example to indicate the three projected component parts, which are L, R, and the chain. (b) The total density of states of devices C4–C9. Projected density of states of devices C4–C9, (c) part L, and (d) part R.

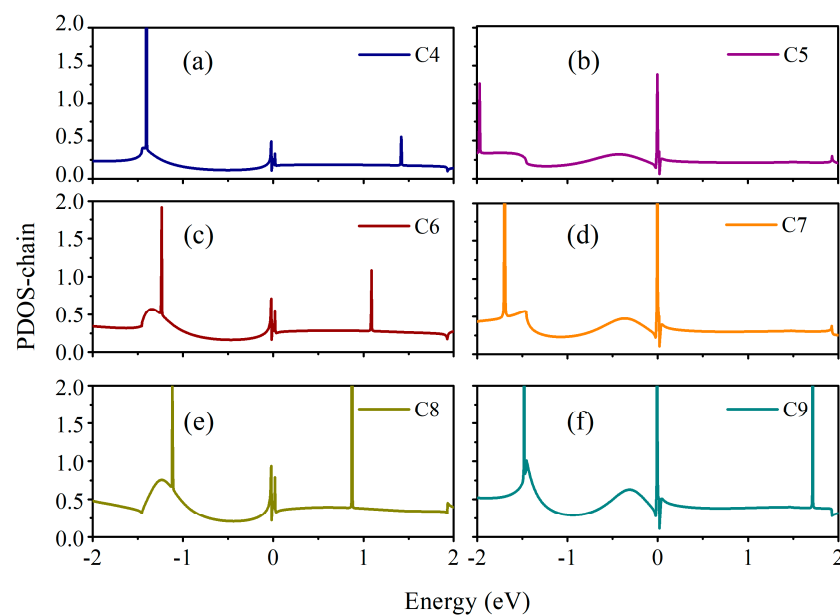


Figure 3. The PDOSchain of devices (a) C4, (b) C5, (c) C6, (d) C7, (e) C8, and (f) C9.

Next, we analyze the ladder-shaped carbon chains in Figure 4a. Each ladder-shaped carbon chain contains $2n$ atoms where n is between four to nine. The structures of six ladder-shaped carbon chain devices, designated as L_n (where n ranges from four to nine), are formed by connecting the terminal atoms of the ladder-shaped carbon chains with the center atoms of the graphene electrodes, positioned along the centerline of the ribbons. After optimization, current–voltage curves for these devices are shown in Figure 4b. The I–V curves for these two-probe ladder-shaped systems can be categorized into two distinct groups. Specifically, devices L5 and L8 exhibit a similar trend, characterized by linear I–V responses. Conversely, for devices L4, L6, L7, and L9, the conductance exhibits a gradual decrease with increasing bias, and the current reaches a saturation point for biases greater than 0.1 V. This behavior suggests that these particular devices hold potential for applications as current stabilizers within electronic circuits.

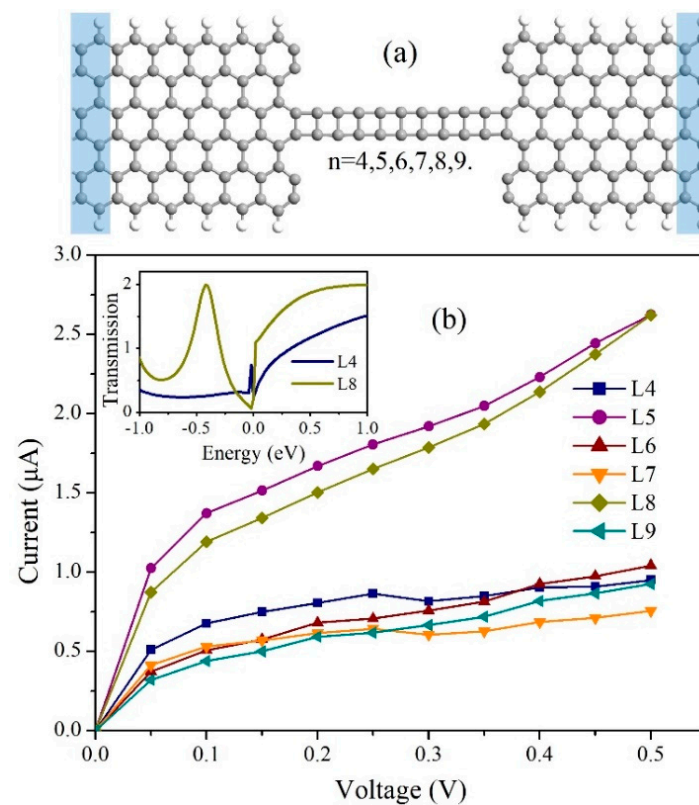


Figure 4. (a) Atomic structure of the ladder-shaped carbon-chain devices. The blue rectangle areas indicate the left and right electrodes, between which is the central scattering region. (b) I–V curves of all the ladder-shaped carbon-chain devices. The inset shows the zero-bias transmission spectra of L4 and L8.

To understand the I–V characteristics distinctively, we select L4 and L8 as representative examples from each group. The zero-bias transmission spectra for these devices are depicted in the inset of Figure 4b. Device L4 exhibits a pronounced resonance peak at the Fermi energy, with a transmission coefficient nearing 0.7, while L8 demonstrates a substantial conductance plateau near and above E_F , with a transmission coefficient around 1.1. This indicates that activating the electronic conduction channels in these devices requires only minimal bias voltage, aligning with their linear I–V responses at lower biases, as corroborated by the data in Figure 4b.

The transmission spectra of L4 and L8 for different bias voltages are plotted in Figure 5. For the L4 structure, the integral of the transmission coefficient within the bias window remains largely constant as the bias voltage increases from 0.1 V to 0.5 V, since the transmission spectra shift congruently with the transport window. Consequently, the current in

the L4 structure plateaus, suggesting its potential utility as a current stabilizer in electronic circuits. Conversely, in the L8 structure, the transport window transitions more rapidly than the transmission spectra, which expands the integral areas pertinent to electron transport and explains the steady current augmentation observed in L8. Comparatively, at the same bias voltages, the integrated transmission coefficient within the bias window is smaller for L4 than for L8, which directly correlates with the observed lower current in L4 compared to L8.

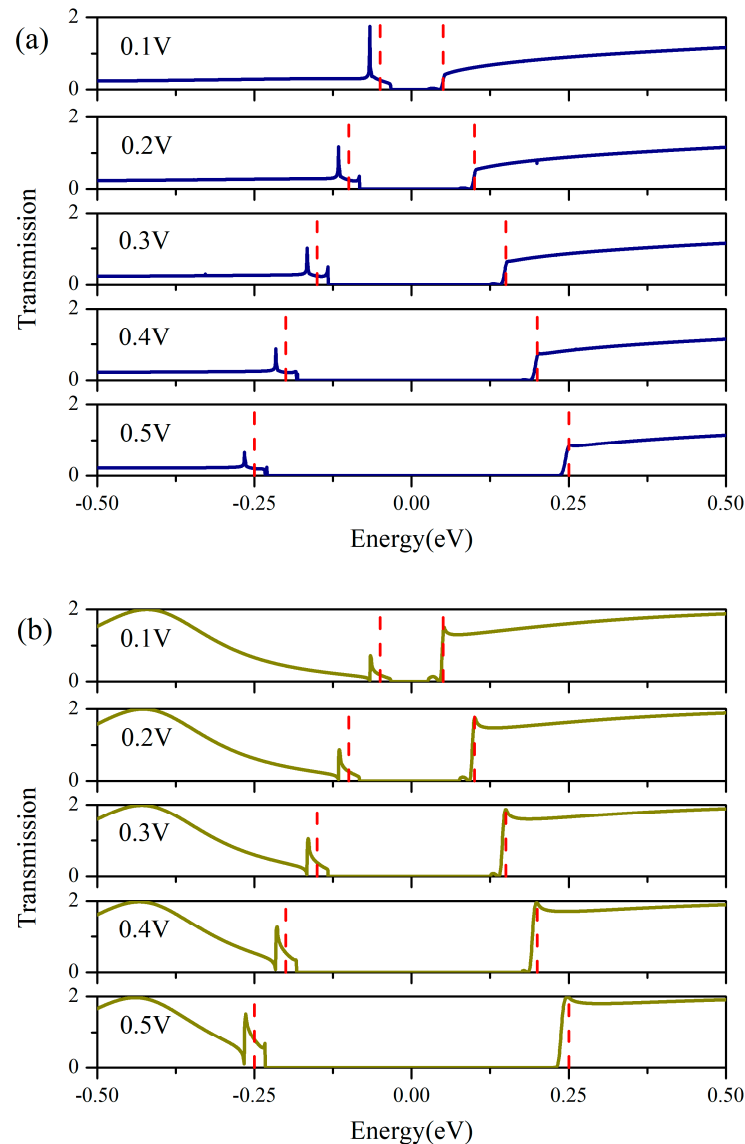


Figure 5. Transmission spectra for (a) device L4 and (b) device L8 under various bias voltages. The red dotted area is the bias window.

To explain the underlying physical mechanism of the current and voltage characteristic curves of L4 and L8, the density of states of L4 and L8 were calculated, as shown in Figure 6. The PDOS-L and PDOS-R of L4 and L8 are almost the same, which is the reason why the TDOSs of L4 and L8 are almost the same. The PDOS-L, PDOS-R, and TDOS between L4 and L8 are much the same, so they cannot explain the difference between the I–V curves of L4 and L8. Figure 6b shows the PDOS-chain of L4 and L8, overall, the value of L8 is greater than that of the L4 near E_F . That is, compared with device L4, there are more carriers involved in electron transport in device L8, so the current of L8 is greater

than the current of L4. Thus, the PDOS-chain is the intrinsic reason why the I–V curves of L4 and L8 differ.

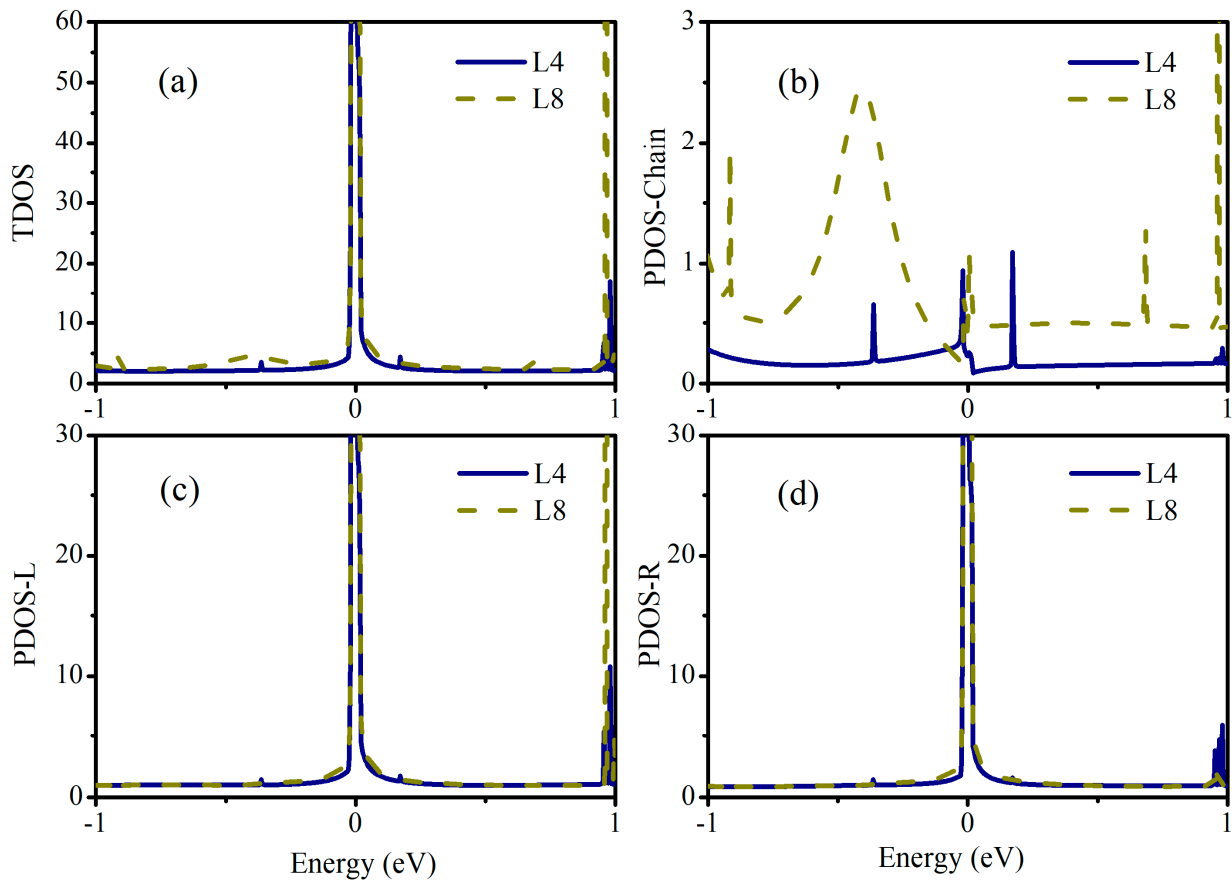


Figure 6. (a) Total density of states of devices L4 and L8. Projected density of states of devices L4 and L8, (b) the chain, (c) part L, and (d) part R.

Following this, we explore devices incorporating a six-membered carbon ring (benzene) connected to ZGNR electrodes through a ladder-shaped carbon chain, as illustrated in Figure 7. The series ranges from D1 to D5, where the benzene ring is sequentially relocated from left to right, and notably, the D3 device configuration exhibits mirror symmetry relative to line AB. The x -axis is aligned with the width of the ZGNR, and the y -axis is oriented perpendicular to the ZGNR plane, with electron transport proceeding along the z -axis. All these systems are characterized by their mirror symmetry with respect to the y - z plane. We construct virtual bulks periodically along the z -axis, which is crucial for the subsequent analysis of the evolution of the electronic states with the movement of the benzene-ring molecule [26]. The virtual bulk consists of a central molecule and four primitive cells of ZGNR in each two-probe device.

The zero-bias transmission spectra of devices D1–D5 are plotted together for comparison, as shown in Figure 8. The symmetrical nature of the device structures—D1 with D5 and D2 with D4—around the central axis AB along the x -direction results in overlapping transmission spectra between D1 and D5, as well as between D2 and D4. Consequently, our analysis will primarily focus on the electron-transport properties of devices D1, D2, and D3. Notably, the distinctions among these devices are predominantly manifested in the spectral region below E_F .

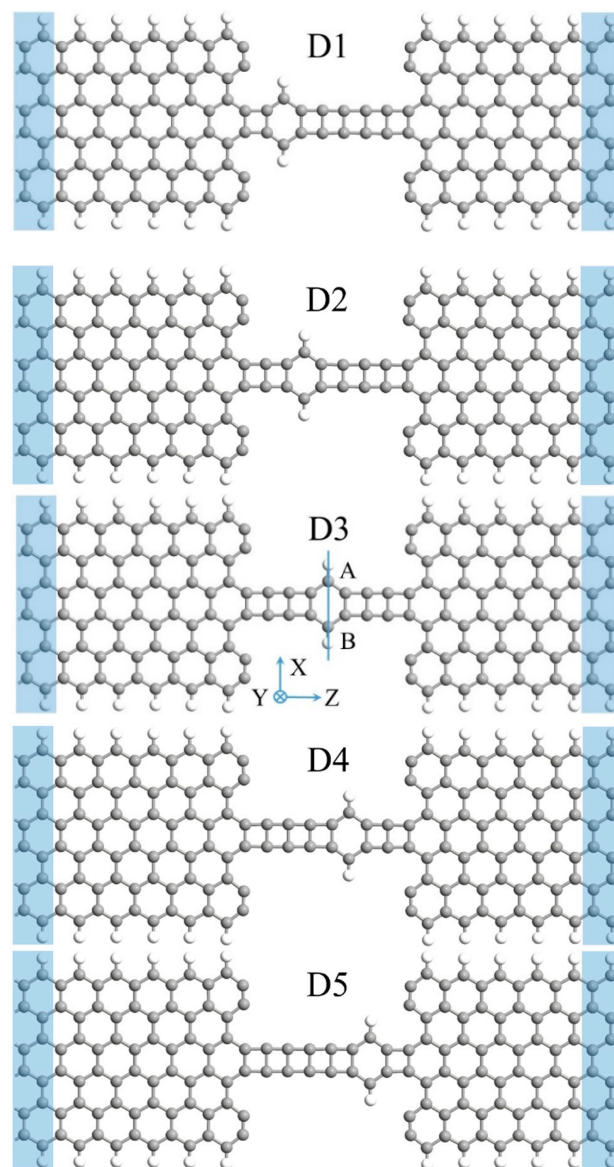


Figure 7. Top view of devices D1–D5. The electron transport is along the z-axis. The blue rectangle areas indicate the left and right electrodes, between which is the central scattering region.

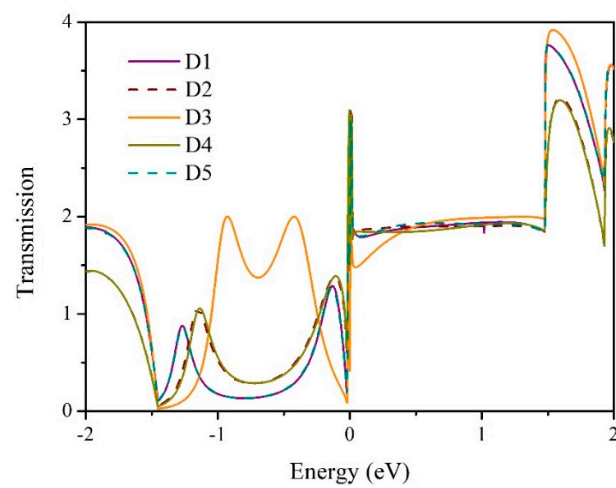


Figure 8. Zero-bias transmission spectra of D1–D5.

In Figure 9a, we present the conductance spectrum of device D1. The molecular energy spectrum for the central molecule are indicated with several red straight lines. Above E_F , there is a wide conductance plateau, and below E_F , two conductance peaks (at -1.26 and -0.14 eV) are observed. The conductance peak at E_F shows characteristics of Fano resonance [31,32]. To figure out the transport modes near E_F , we plot the energy bands of the virtual bulk corresponding to D1 in Figure 9b and present the wave functions in Figure 10 to show the corresponding transport modes.

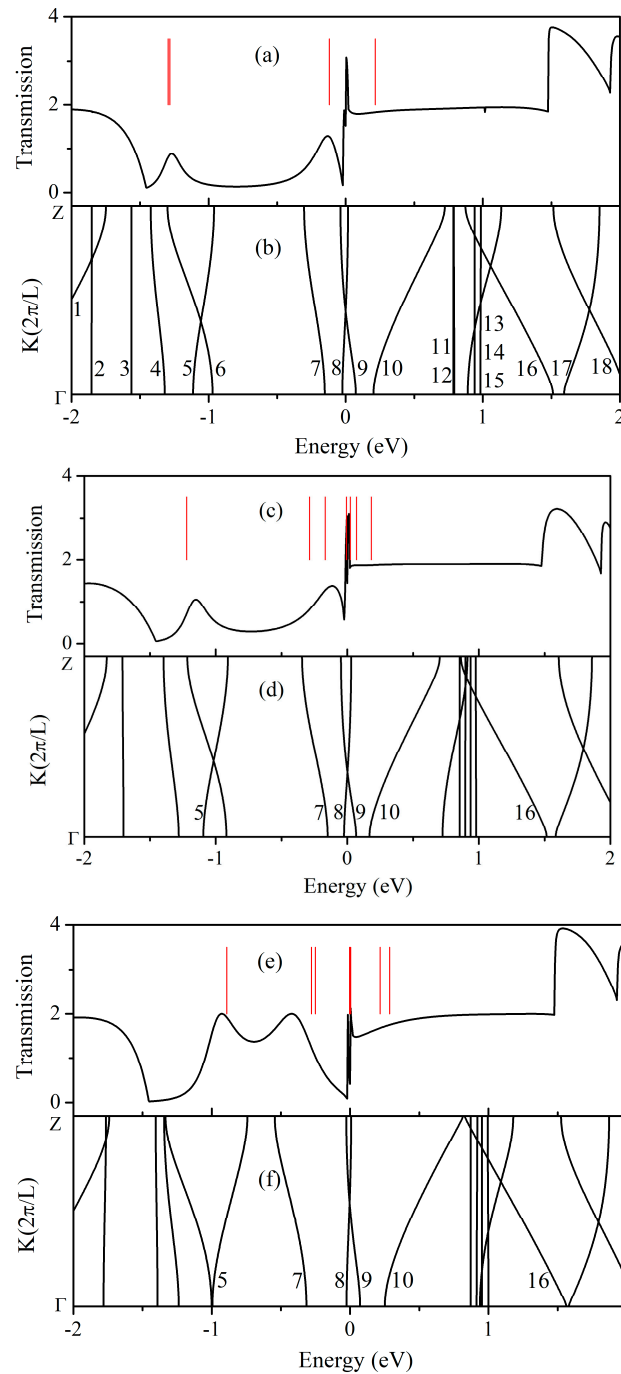


Figure 9. Conductance spectra of devices D1, D2, and D3 are plotted in (a,c,e), respectively. The molecular-energy spectra for the central molecule corresponding to each device are indicated with several red straight lines. The energy bands of the virtual bulks corresponding to devices D1, D2, and D3 are presented in (b,d,f), respectively. In devices D2 and D3, some bands corresponding to the bands of device D1 are marked with the same numbers as device D1.

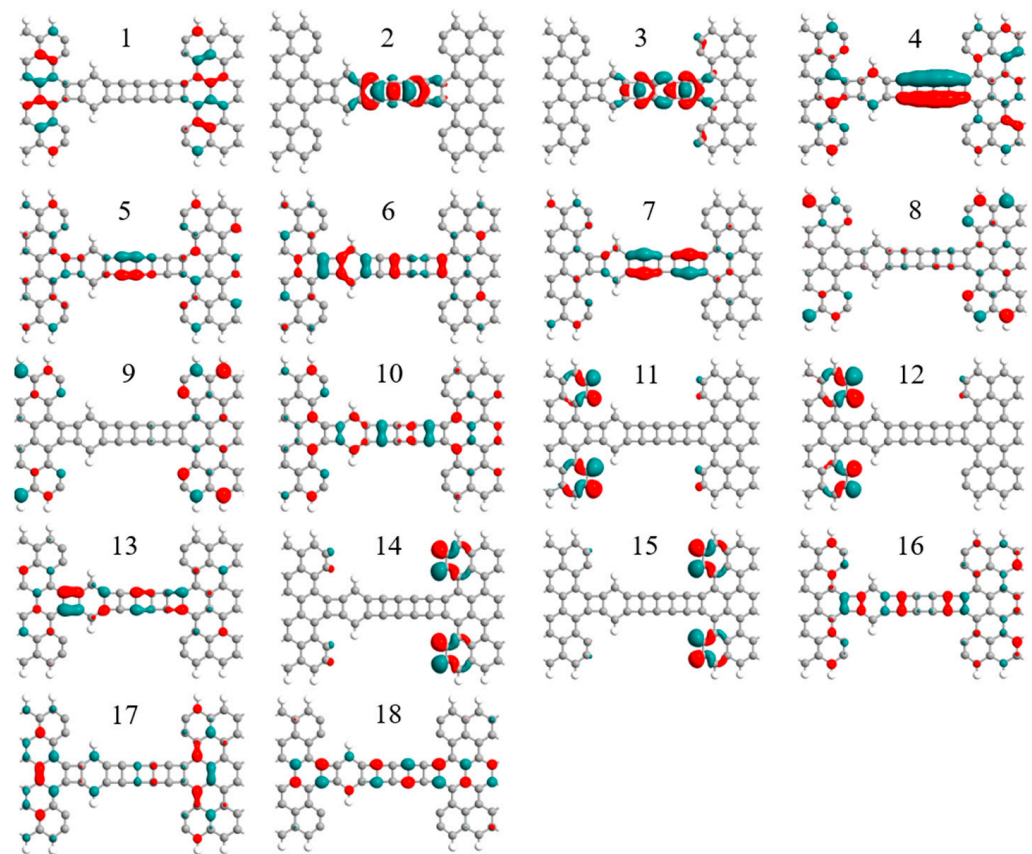


Figure 10. The wave function for $k = 0$ states in each and every band of the virtual bulk corresponding to device D1.

For the states in band 1 (transport mode 1), nine are mainly localized in the electrodes. The states in bands 2 and 3 are mainly confined to the chain with symmetric parity. The states in bands 11, 12, 14, and 15 correspond to the dangling orbitals at the end of the electrodes and are localized. These modes cannot transport a charge in the two-probe device D1. The states in bands 6, 10, 16, and 17 are all symmetric in both the central molecule and ZGNRs but have different patterns. The states in 4, 5, 7, 8, 13, and 18 have antisymmetric parity. These modes can transport a charge in the two-probe device D1.

The two-probe system can be described as the central molecular electron levels sandwiched between ZGNR bands. The wave function of states (β and α) near and below E_F in ZGNRs has antisymmetric parity, and the wave function of states (γ and δ) near and above E_F in ZGNRs has symmetric parity, as shown in Figure 11b. There are four levels in the central molecule in the energy range $(-2, 2)$ eV, which are LUMO, HOMO, HOMO-1, and HOMO-2, as shown in Figure 11c. The wave functions of LUMO and HOMO-1 have mirror symmetry with respect to the y - z plane, and the wave functions of HOMO and HOMO-2 display antisymmetry. The wave function of HOMO-1 combines with band α , and the bond between the wave functions of the two atoms of the electrodes in the contact point has no symmetric component; under this circumstance the two-probe device D1 cannot transport the charge. On the contrary, the wave function of HOMO-2 combines with band α and can transport the charge. Although the HOMO wave function is localized at the right end of the molecule, it will be reorganized after binding with the electrode, so D1 can also transport electrons after combining the HOMO state and the wave function of band α . As a result, there are two transmission peaks below E_F .

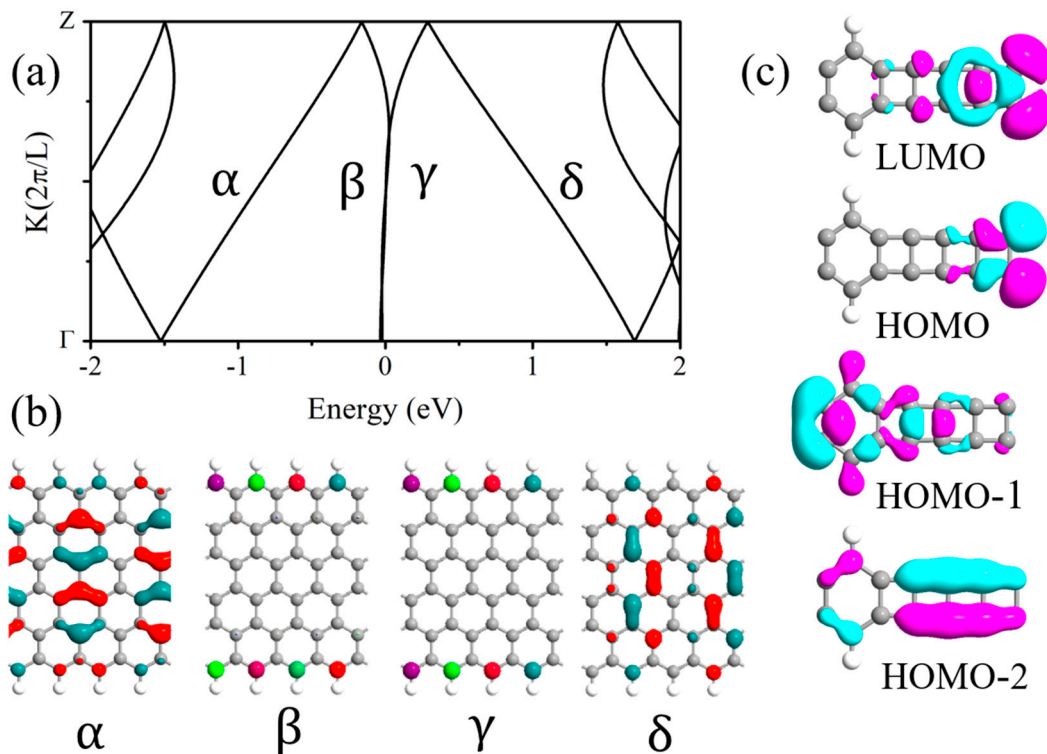


Figure 11. (a) Energy bands of a 6-ZGNR bulk calculated with unit cell of four primitive cells. (b) The wave function of the four bands. (c) The wave functions of LUMO, HOMO, HOMO-1, and HOMO-2 of the central molecule of device D1.

With the help of the electronic energy bands and the wave functions in the virtual bulk of D1, we obtain the corresponding transport modes. The peak at -1.26 eV comes from transport mode 5 and the peak at -0.14 eV comes from transport mode 7. This is confirmed by the calculation of the transport modes at $E = -1.26, -0.14$ eV, as shown in Figure S1. The state in band 5 is composed of the HOMO-2 state in the central molecule. Above E_F , the wide conductance plateau corresponds to transport mode 10 and 16. The conductance peak at E_F shows characteristics of Fano resonance due to the weak coupling between the extending modes 7 and 10 and the localized modes 8 and 9.

According to the data analysis of the electronic band structure and wave function of the virtual cell of device D2, the two transmission peaks at -1.15 eV and -0.12 eV correspond to band 5 and band 7. Compared with the wave function of the central molecule, the wave function of band 5 of device D2 is provided by the HOMO-3 state, as shown in Figure S2. The wide conductivity spectrum above E_F corresponds to bands 10 and 16. The wave function of band 10 is provided by the LUMO+1 state of the central molecule. The origin of the Fano resonance peak is similar to that of device D1.

In device D3, the transmission peaks at -0.93 eV and -0.42 eV come from band 5 and band 7, respectively. The wave function of band 5 is composed of the HOMO-3 state of the central molecule, and the wave function of band 7 is composed of the LUMO state of the central molecule, as shown in Figure S3. The wide conductivity spectrum above E_F corresponds to bands 10 and 16. The wave function of band 10 is composed of the LUMO+2 state of the central molecule. Compared to devices D1 and D2, band 7 and band 10 are further away from E_F , resulting in a weaker coupling between extended energy bands 7 and 10 and localized energy bands 8 and 9; for this reason, the Fano resonance peak of device D3 is lower than that of devices D1 and D2.

We calculated the current–voltage characteristic curves of five devices D1–D5 at 0 V–0.5 V, as shown in Figure 12. The following characteristics can be seen from the figure: First, in the voltage region (0 V–0.15 V), D1–D5 devices have similar current and voltage

characteristics. When the voltage is very small, the current of D1–D5 structures increases rapidly, and the current-growth trend slows down with the increase in voltage. Second, when the voltage is greater than 0.15 V, the current of D1 and D4 remains stable in the voltage range of (0.15 V–0.2 V). When the voltage is greater than 0.2 V, the current of D1 and D4 slowly decreases with the increase in voltage, resulting in NDR. And D1 decreases faster, with a small current peak at 0.45 V, so D1 has a double NDR over the entire bias range. The transmission spectra and the chemical potential window open simultaneously, the tempo competition between them resulting in the double NDR of D1, as shown in Figure S4. Third, the current of both D2 and D5 continues to increase in the voltage range (0 V–0.4 V), then slowly decreases at the same time; both D2 and D5 show NDR. At last, D3's current continues to grow throughout the voltage range and is the smallest of the five structures at less than 0.35 V, owing to the integral area in the bias window of D3 being the smallest, as shown in Figure S5. After which, it gradually surpasses D1 and D4.

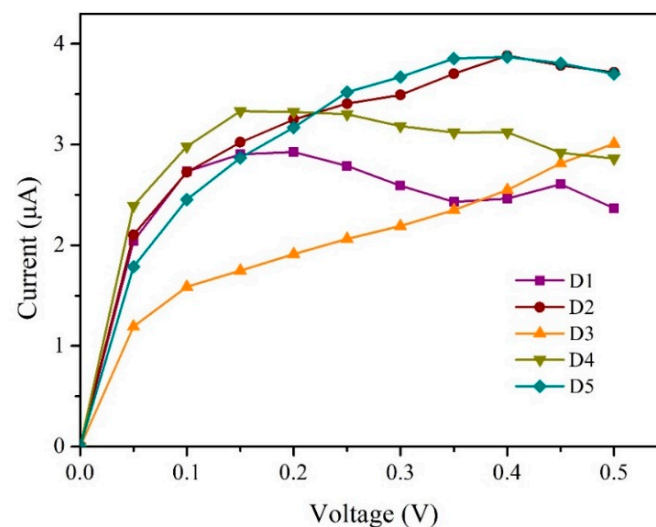


Figure 12. I–V curves of D1–D5.

In the part below E_F , band 5 shifts to the right as the benzene ring moves from left to right, causing the left transmission peak shifts to the right. Compared with energy band 7 of devices D1 and D2, energy band 7 of device D3 has a large shift to the left, so the right transmission peak of device D3 has a large shift to the left. The electron states of the central molecule and their matching to the states in the electrodes change as the benzene-ring molecule moves, which can lead to the movement of the energy bands of the virtual bulk, in which the change in the transmission peaks of the transmission spectrum ensues, hence the position of NDR shifts in the low-bias region (0 to 0.5 V). Therefore, the electron states of the central molecule and their matching to the states in the electrodes dominate the transmission spectra and I–V characteristics of devices D1–D5.

4. Conclusions

By applying the density functional theory, combined with the non-equilibrium Green's function approach, we conducted comprehensive investigations into the electronic transport properties of carbon-chain-based molecular devices at low biases. In devices composed of atomic carbon chains of varying lengths connected to graphene nanoribbon (GNR) electrodes, a pronounced even–odd current behavior was observed, with the linear and consistent currents suggested Ohmic contact characteristics. Next, devices incorporating GNR electrodes connected by ladder-shaped carbon chains exhibited distinct current-stabilizing behavior, demonstrating their potential as current stabilizers in electronic circuits. Furthermore, molecular devices that integrate a ladder-shaped carbon chain with a benzene-ring molecule displayed a negative differential resistance (NDR) effect at low-bias voltages. Detailed analyses of the energy bands of virtual bulks, the molecular energy spectrum,

wave functions, and transmission spectra under various external voltage biases offer deep insights into the underlying mechanisms of the observed phenomena, revealing that the tunable NDR stems from alterations in the electron states of the central molecule and their alignment with the electrode states. This research provides valuable insights into the potential applications and functional versatility of atom-chain-based devices.

Supplementary Materials: The following supporting information can be downloaded at <https://www.mdpi.com/article/10.3390/electronics13091764/s1>, Figure S1: For D1: The transport modes at $E = -1.26, -0.14$ eV and the wave functions for $k = 0$ states in bands 5 and 7 are presented correspondingly; Figure S2: For D2: The transport modes at $E = -1.15, -0.12$ eV; the wave functions for $k = 0$ states in bands 5, 7, 8, 9, 10 and 16; the wave functions of LUMO+1 and HOMO-3 of central molecule; Figure S3: For D3: The transport modes at $E = -0.93, -0.42$ eV; the wave functions for $k = 0$ states in bands 5, 7, 8, 9, 10 and 16; the wave functions of LUMO+2, LUMO and HOMO-3 of central molecule; Figure S4: Transmission spectra of D1 at different bias voltage; Figure S5: 0.15 V-bias-transmission spectra of D1–D5.

Author Contributions: Conceptualization, L.W., L.Z. and X.W.; methodology, L.W.; formal analysis, L.W.; writing—original draft preparation, L.W.; writing—review and editing, W.Y., L.Z. and X.W.; funding acquisition, L.Z. and X.W. All authors have read and agreed to the published version of the manuscript.

Funding: This research was funded by the National Natural Science Foundation of China grant number 62274113 and 61674110.

Data Availability Statement: The original contributions presented in the study are included in the article/Supplementary Materials, further inquiries can be directed to the corresponding authors.

Conflicts of Interest: The authors declare no conflicts of interest.

References

1. Pan, J.B.; Zhang, Z.H.; Deng, X.Q.; Qiu, M.; Guo, C. The Transport Properties of D- σ -A Molecules: A Strikingly Opposite Directional Rectification. *Appl. Phys. Lett.* **2011**, *98*, 013503. [CrossRef]
2. Chen, T.; Yan, S.; Xu, L.; Liu, D.; Li, Q.; Wang, L.; Long, M. Spin-Filtering and Giant Magnetoresistance Effects in Polyacetylene-Based Molecular Devices. *J. Appl. Phys.* **2017**, *122*, 035103. [CrossRef]
3. Imai-Imada, M.; Imada, H.; Miwa, K.; Tanaka, Y.; Kimura, K.; Zoh, I.; Jaculbia, R.B.; Yoshino, H.; Muranaka, A.; Uchiyama, M.; et al. Orbital-Resolved Visualization of Single-Molecule Photocurrent Channels. *Nature* **2022**, *603*, 829–834. [CrossRef] [PubMed]
4. Yanson, A.I.; Bollinger, G.R.; van den Brom, H.E.; Agrait, N.; van Ruitenbeek, J.M. Formation and Manipulation of a Metallic Wire of Single Gold Atoms. *Nature* **1998**, *395*, 783–785. [CrossRef]
5. Zeng, J.; Chen, K.-Q. Abnormal Oscillatory Conductance and Strong Odd–Even Dependence of a Perfect Spin-Filtering Effect in a Carbon Chain-Based Spintronic Device. *J. Mater. Chem. C* **2015**, *3*, 5697–5702. [CrossRef]
6. Zhou, Y.; Li, Y.; Li, J.; Dong, J.; Li, H. Electronic Transport Properties of Carbon and Boron Nitride Chain Heterojunctions. *J. Mater. Chem. C* **2017**, *5*, 1165–1178. [CrossRef]
7. Kim, H.S.; Kim, T.H.; Kim, Y.-H. Odd-Even Phonon Transport Effects in Strained Carbon Atomic Chains Bridging Graphene Nanoribbon Electrodes. *Carbon* **2019**, *142*, 107–114. [CrossRef]
8. Xu, X.; Li, W.; Liu, L.; Feng, J.; Jiang, Y.; Tian, W.Q. Implementation of Outstanding Electronic Transport in Polar Covalent Boron Nitride Atomic Chains: Another Extraordinary Odd-Even Behaviour. *Sci. Rep.* **2016**, *6*, 26389. [CrossRef] [PubMed]
9. Xu, Y.; Ke, S.-H. Reversed Even-Odd Oscillation of Spin-Polarized Equilibrium Conductance in an All-Carbon Junction. *J. Appl. Phys.* **2019**, *125*, 234301. [CrossRef]
10. Mu, Y.; Zhou, Y.; Zhang, T.; Zeng, Z.-Y.; Cheng, Y. Electronic Transport of (SiC)_n ($n = 1-4$) Molecular Chains via First-Principles Calculations. *J. Chem. Eng. Data* **2017**, *62*, 3889–3902. [CrossRef]
11. Deng, X.Q.; Zhou, J.C.; Zhang, Z.H.; Zhang, H.; Qiu, M.; Tang, G.P. Electrode Conformation-Induced Negative Differential Resistance and Rectifying Performance in a Molecular Device. *Appl. Phys. Lett.* **2009**, *95*, 163109. [CrossRef]
12. Qiu, M.; Li, J.; Liew, K.M.; Yuan, C. Rectifying Performance and Negative Differential Behavior in Graphite-Chain-Carbon Nanotube Junctions. *Appl. Phys. Lett.* **2014**, *104*, 023102. [CrossRef]
13. Zhang, Z.H.; Guo, C.; Kwong, G.; Deng, X.Q. Electronic Transport of Nitrogen-Capped Monoatomic Carbon Wires between Lithium Electrodes. *Carbon* **2013**, *51*, 313–321. [CrossRef]
14. Janatipour, N.; Mahdavi, Z.; Noorzadeh, S.; Schreckenbach, G. Achieved Negative Differential Resistance Behavior of Si/B-Substituted into a C₆ Chain Sandwiched between Capped Carbon Nanotube Junctions. *RSC Adv.* **2022**, *12*, 1758–1768. [CrossRef]

15. Larade, B.; Taylor, J.; Mehrez, H.; Guo, H. Conductance, I – V Curves, and Negative Differential Resistance of Carbon Atomic Wires. *Phys. Rev. B* **2001**, *64*, 075420. [[CrossRef](#)]
16. Khoo, K.H.; Neaton, J.B.; Son, Y.W.; Cohen, M.L.; Louie, S.G. Negative Differential Resistance in Carbon Atomic Wire-Carbon Nanotube Junctions. *Nano Lett.* **2008**, *8*, 2900–2905. [[CrossRef](#)] [[PubMed](#)]
17. Zhou, Y.-H.; Chen, C.-Y.; Li, B.-L.; Chen, K.-Q. Characteristics of Classical Kirchoff’s Superposition Law in Carbon Atomic Wires Connected in Parallel. *Carbon* **2015**, *95*, 503–510. [[CrossRef](#)]
18. Mu, Y.; Lan, J.-Q.; Zhou, X.-L.; Chen, Q.-F. Electronic Transport of SiC Molecular Chains in Parallel via First-Principles Calculations. *J. Appl. Phys.* **2019**, *125*, 204301. [[CrossRef](#)]
19. Mu, Y.; Yu, J.; Hu, R.; Wang, C.-H.; Cheng, C.; Hou, B.-P. Ab Initio Study Revealing Remarkable Oscillatory Effects and Negative Differential Resistance in the Molecular Device of Silicon Carbide Chains. *Phys. Chem. Chem. Phys.* **2023**, *25*, 13265–13274. [[CrossRef](#)]
20. Yun, J.; An, H.; Huang, R.; Guo, M.; Zhang, Y.; Kang, P. Interesting Odd–Even Effect, Ohmic Contact, Negative Differential Resistance, and Current Stabilizer Behavior in All-Carbon Graphyne/Carbon-Chain Junctions. *IEEE Trans. Electron Devices* **2020**, *67*, 2529–2535. [[CrossRef](#)]
21. Wan, H.; Zhou, B.; Chen, X.; Sun, C.Q.; Zhou, G. Switching, Dual Spin-Filtering Effects, and Negative Differential Resistance in a Carbon-Based Molecular Device. *J. Phys. Chem. C* **2012**, *116*, 2570–2574. [[CrossRef](#)]
22. Han, X.; Yang, J.; Yuan, P.; Bian, B. Spin-Dependent Transport in All-Carbon Multifunctional Spintronic Device. *Eur. Phys. J. B* **2019**, *92*, 32. [[CrossRef](#)]
23. Vazquez, H.; Skouta, R.; Schneebeli, S.; Kamenetska, M.; Breslow, R.; Venkataraman, L.; Hybertsen, M.S. Probing the Conductance Superposition Law in Single-Molecule Circuits with Parallel Paths. *Nat. Nanotechnol.* **2012**, *7*, 663–667. [[CrossRef](#)] [[PubMed](#)]
24. Mu, Y.-Q.; Zhao, J.-M.; Chen, L.-Y.; Huang, H.; Wang, M.-L.; Hu, G.-C.; Wang, C.-K.; Zhang, G.-P. Odd-Even Effect of the Switching Performance for Dimethyldihydropyrene/Cyclophanediene Single-Molecule Switch Modulated by Carbon Atomic Chains. *Org. Electron.* **2020**, *81*, 105665. [[CrossRef](#)]
25. Tang, X.-J.; Xia, C.-J.; Fang, Q.-L.; Hu, Z.-Y.; Yu, J.; Zhang, T.-T. Negative Differential Resistance in Oligomeric Phenylene Ethynyls Molecular Device with C 2 N-h2D Nanoribbon Electrodes. *Jpn. J. Appl. Phys.* **2020**, *59*, 126001. [[CrossRef](#)]
26. Yao, A.-L.; Dong, Y.-J.; Wang, X.-F.; Liu, Y.-S. Electron Transport through Phenylene Sandwiched between Zigzag Graphene Nanoribbons. *Appl. Nanosci.* **2019**, *9*, 143–149. [[CrossRef](#)]
27. Wan, H.; Xu, Y.; Zhou, G. Dual Conductance, Negative Differential Resistance, and Rectifying Behavior in a Molecular Device Modulated by Side Groups. *J. Chem. Phys.* **2012**, *136*, 184704. [[CrossRef](#)]
28. Zhang, Z.; Guo, C.; Kwong, D.J.; Li, J.; Deng, X.; Fan, Z. A Dramatic Odd–Even Oscillating Behavior for the Current Rectification and Negative Differential Resistance in Carbon-Chain-Modified Donor–Acceptor Molecular Devices. *Adv. Funct. Mater.* **2013**, *23*, 2765–2774. [[CrossRef](#)]
29. Brandbyge, M.; Mozos, J.-L.; Ordejón, P.; Taylor, J.; Stokbro, K. Density-Functional Method for Nonequilibrium Electron Transport. *Phys. Rev. B* **2002**, *65*, 165401. [[CrossRef](#)]
30. Jauho, A.-P.; Wingreen, N.S.; Meir, Y. Time-Dependent Transport in Interacting and Noninteracting Resonant-Tunneling Systems. *Phys. Rev. B* **1994**, *50*, 5528–5544. [[CrossRef](#)]
31. Yang, X.F.; Kuang, Y.W.; Liu, Y.S.; Zhang, D.B.; Shao, Z.G.; Yu, H.L.; Hong, X.K.; Feng, J.F.; Chen, X.S.; Wang, X.F. Carbon-Based Molecular Devices: Fano Effects Controlled by the Molecule Length and the Gate Voltage. *Nanoscale* **2016**, *8*, 15712–15719. [[CrossRef](#)] [[PubMed](#)]
32. Liu, Y.-S.; Zhang, X.; Feng, J.-F.; Wang, X.-F. Spin-Resolved Fano Resonances Induced Large Spin Seebeck Effects in Graphene-Carbon-Chain Junctions. *Appl. Phys. Lett.* **2014**, *104*, 242412. [[CrossRef](#)]

Disclaimer/Publisher’s Note: The statements, opinions and data contained in all publications are solely those of the individual author(s) and contributor(s) and not of MDPI and/or the editor(s). MDPI and/or the editor(s) disclaim responsibility for any injury to people or property resulting from any ideas, methods, instructions or products referred to in the content.